metals

MDPI

Article

Ab Initio-Based Modelling of the Yield Strength in High-Manganese Steels

Simon Sevsek * and Wolfgang Bleck

Steel Institute, RWTH Aachen University, Intzestraße 1, 52072 Aachen, Germany; bleck@iehk.rwth-aachen.de
* Correspondence: simon.sevsek@iehk.rwth-aachen.de; Tel.: +49-241-80-90138

Received: 15 November 2017; Accepted: 3 January 2018; Published: 5 January 2018

Abstract: An ab initio-based model for the strength increase by short-range ordering of C-Mn-Al clusters has been developed. The model is based on ab initio calculations of ordering energies. The impact of clusters on the yield strength of high-manganese austenitic steels (HMnS) is highly dependent on the configurational structure of the cells that carbon atoms will position themselves as interstitial atoms. The impact of the alloying elements C, Mn, and Al on the potential and actual increase in yield strength is analyzed. A model for the calculation of yield strengths of HMnS is derived that includes the impact of short-range ordering, grain size refinement, and solid solution strengthening. The model is in good agreement with experimental data and performs better than other models that do not include strengthening by short-range ordering.

Keywords: short-range ordering; yield strength; high-manganese steel

1. Introduction

High Mn austenitic steels (HMnS) offer great combinations of hardness and ductility with a wide range of possible applications in various industries, such as the automotive industry [1–3]. Depending on the stacking fault energy, which is a result of alloying content, temperature, deformation grade, and other factors, HMnS exhibit a variety of different active deformation modes [4–7]. Those deformation modes include transformation induced plasticity (TRIP), twinning-induced plasticity (TWIP) or pronounced planar glide in combination with the formation of dislocation cells that is sometimes referred to as microband-induced plasticity (MBIP) [1,8–10]. The mode of deformation significantly influences the level of work hardening and plays a major role in determining the mechanical properties [7]. One of those material characteristics is the material's yield strength (YS). In the past, various attempts have been made to model the YS of HMnS based on the chemical composition using linear regression [5,11–13]. However, these models often imply negative solid-solution strengthening by some of the alloying elements, like Mn, that are usually attributed to positive strengthening effects [2,14,15].

Interactions of carbon-metal pairs [16–18] and clusters are described by the concept of short-range ordering (SRO) phenomena [19] in HMnS and might offer an explanation for an additional increase in strength that might lead to a defective linear regression when using standard methods to calculate the impact of solid solution strengthening [14,20,21]. Short-range ordered clusters are a result of local differences in ordering energies that make particular unit cell configurations preferential to inhibit a carbon atom [22]. Ab initio calculations employing density-functional theory (DFT) have been shown to be suitable for calculations of ordering energies in HMnS for several chemical compositions. For example, thermodynamic predictions of κ-phase stability [23], interface energies [24], stacking fault energies [25], and hydrogen trap sites [26] showed good agreement with the experimental data.

Cell models [27] have been used to determine the location of carbon atoms in relation to the matrix or substitutional alloying atoms. Other studies show that the interaction of carbon atoms with

each other is very repulsive and, thus, influences the diffusion behavior [4,25,28–30], which also points to a coordination of carbon atoms in octahedral sites dependent of surrounding solute atoms. Additionally, the position of C also influences the stacking fault energy of the material [31].

Short-range ordering has also been used to explain the pronounced planar glide that HMnS exhibit because of glide plane softening that occurs when short-range ordered C-Mn clusters are destroyed by dislocation stresses reorienting the carbon atom from its octahedral position to a tetrahedral position. This phenomenon also explains the serrated flow curves that can be found during tensile testing of HMnS, as the back stresses of dislocation pile-ups lead to an increase in strength. The reorientation of the carbon atom then leads to a temporary destruction of the short-range ordered cluster and as a result, a rapid drop in strength because of subsequent softening of this glide plane [32]. However, short-range ordering can be restored by short-range jumps of C back from the tetrahedral site to its initial octahedral site [1,2]. Those short-range jumps might be activated by temperature, but already occur at low temperatures where diffusion processes are usually negligible [1,32].

In this study, a basic cell model for the nearest-neighboring atoms of a central octahedral carbon atom is expanded to include the corner atoms of an elementary cell of an austenitic face-centered cubic (FCC) unit cell, which can be described as the second-nearest neighbors of the central octahedral site in an austenitic cell [27]. Results of ab initio calculations are employed to show that the position of Mn and Al being coordinated as a nearest neighbor or second-nearest neighbor to a central carbon atom is of major importance to the energy level of the system [33]. It is assumed that this also holds true in the case of a central interstitial nitrogen atom [2,33,34] but, in this work, the authors will focus solely on carbon. Based on the calculated ordering energies, the yield strength of HMnS is a result of a combination of short-range ordered clusters, regular solid-solution hardening, grain size effects, and the base strength of an austenitic lattice [14,35].

2. Materials and Methods

Many models for the calculation of the yield strength of austenitic steels have been published in the past. Those models generally employ two mechanisms to describe the yield strength: a strengthening by grain size reduction, the Hall-Petch effect, and the alloying elements' contribution to the material's strength [15,36,37]. Many of those models have used databases with significant amounts of different alloys to employ a linear regression in order to get parameters that determine the effect of alloying elements on the yield strength of the austenitic steel. Assuming that SRO in HMnS influences the yield strength σ_Y significantly, a term describing this effect has to be added to the equation [14], resulting in:

$$\sigma_Y = \sigma_0 + \sigma_{SS} + \sigma_{GS} + \sigma_{SRO} \tag{1}$$

where σ_0 is the base strength of a pure austenitic iron lattice and is assumed to be 90 MPa [14]. σ_{SS} is the contribution of alloying elements to the change in yield strength relative to a pure austenitic lattice. Since this paper focuses on HMnS with the main alloying elements C, Mn, and Al, those elements are assumed to be the main contributors to solid solution strengthening and the contributions of other alloying elements are neglected. It is assumed that this does not lead to a large mistake in calculating σ_{SS} because, apart from Mn and Al, no substitutional alloying element exceeds alloying contents of more than 1 wt. %.

σ_{SRO} is the change in yield strength stemming from the existence of short-range ordered regions in the material. Based on the work of [14], this contribution to yield strength can be calculated as:

$$\sigma_{SRO} = M\tau_{SRO} = M\left(\frac{E_{Order}}{b^3}\right) = M\left(\frac{E_{random} - E_{SRO}}{b^3}\right) \tag{2}$$

where $M = 3.06$ is the Taylor-factor for fcc with $b = \frac{\alpha_\gamma}{\sqrt{2}}$ being the magnitude of the Burgers vector and the lattice parameter in austenite in Å depending on the molar fractions x_i of the alloying elements and temperature in K [38]:

$$\alpha_\gamma = \begin{pmatrix} 3.5780 + 0.033x_C + 0.00095x_{Mn} - 0.0002x_{Ni} \\ + 0.0006x_{Cr} + 0.0056x_{Al} + 0.0031x_{Mo} + 0.0018x_V \end{pmatrix} \times \left(1 + 2.065 \times 10^{-9} \times (\mathrm{T} - 300)\right) \quad (3)$$

Looking at Equation (3), the temperature dependence of the lattice parameter is assumed to be linear.

σ_{GS} describes the strengthening by grain refinement in accordance with the Hall-Petch effect and can be formulated as:

$$\sigma_{GS} = k_y d^{-1/2} \quad (4)$$

Even though k_y depends on the cooling procedure and the carbon content [39], the value $k_y = 11.3$ MPa mm$^{1/2}$ seems to be a reasonable assumption for HMnS in general, based on the findings in the literature [1,2,14,39–41].

As can be seen in Figure 1, one unit cell consists of 14 atoms situated on the lattice positions of the FCC bracket and one central octahedral interstitial site, where a single carbon atom can be situated.

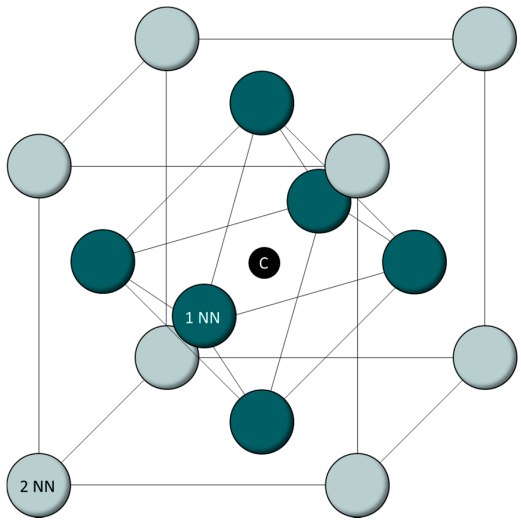

Figure 1. FCC-unit cell with 14 lattice positions for matrix atoms and one central interstitial atom.

First-nearest neighbors (1NN) are the six direct neighbors of the carbon atom. In Figure 1, they are shown in green. Second-nearest neighbors (2NN) in this model are the grey atoms on the corners of the FCC lattice. Although third-nearest neighbors (3NN) can be included in first-principle calculations, a recent study has shown that neither 3NN Al atoms nor 3NN Mn atoms have a positive impact o the ordering energy [33]. To reduce the complexity of the calculations and limit the amount of possible cell configurations, the presence of 3NN alloying atoms is not accounted for in the analysis carried out in this paper. Instead, it is assumed that the material is the sum of FCC-unit cells that do not impact each other. This is obviously not true in reality, but for the purposes of this study, which is aimed at providing a basic model to connect ab initio calculations with experimental results, it is suitable, since it leads to reduced mathematical complexities. The term "cell configuration" is used to describe the combination of alloying atoms and matrix atoms in the cell. "Coordination sphere" is used throughout this paper to refer to the position of atoms relative to the central carbon atom.

The configurations of the cells based on the alloying contents for this 14-cell model are calculated according to [27]:

$$n_{kl} = \frac{14!}{(14 - k - l)!k!l!} \theta_{Fe}^{(14 - k - l)} \theta_{Mn}^{k} \theta_{Al}^{l} \quad (5)$$

where n_{kl} is the fraction of all cells that have a configuration with k Mn atoms and l Al atoms with θ_i being the molar fraction of Fe, Mn, and Al, denying the existence of other substitutional alloying elements and ignoring C, since carbon is an interstitial alloying element. Since diffusion rates of substitutional atoms in austenitic steels are very low, it is assumed that the distribution of substitutional elements according to Equation (5) is fixed and that the carbon atom is distributed in accordance with a minimum ordering energy. For clusters of nitrogen and chromium, this approach has been shown to be a realistic approximation, since the presence of nitrogen does not negatively influence the homogeneous distribution of chromium [34]. Cells of type n_{kl} that contain a carbon atom are classified as n_{Ckl}. It should be noted that the assumption that substitutional atoms are distributed according to minimum ordering energies with respect to the presence of a central carbon atom is a very strong assumption, which is unlikely to be true in reality. However, without this assumption, the calculation of ordering energies ΔE_{Ckl} is not possible since ab initio results are presently not available for those unfavorable configurations.

The ordering energy ΔE_{Ckl} of a cell with k Mn atoms, l Al atoms and a central carbon atom is the combination of two energy contributions in comparison to a FCC-unit cell consisting only of Fe atoms and a central interstitial carbon atom. First, the energy required to bring a carbon atom in solution ΔE_{Sol} in a FCC-unit cell with respect to the presence of k Mn atoms and l Al atoms in the first two coordination spheres. The second factor is the change in energy level ΔE_{Lat} resulting from a lattice distortion due to the presence of Mn and Al:

$$\Delta E_{Ckl} = \Delta E_{Sol} + \Delta E_{Lat} \tag{6}$$

Ab initio calculations show that Al is preferentially situated in the second coordination sphere and Mn has a positive effect on the ordering energy level if it sits on a lattice position as a 1NN [22,25,33]. According to those studies, this means that the difference in ordering energy is so profound that the likelihood of a cell configuration that contains 1NN Al atoms instead of 2NN Al atoms or 2NN Mn atoms instead of 1NN Mn atoms is very low. Accordingly, for further calculations in this work and to reduce the model's complexity, it is assumed that for any number of Mn atoms up to six, they will always be 1NN and for any number of Al atoms up to 8, they will always be 2NN.

Using the calculated ordering energies ΔE_{Ckl} from [33], the six cells with the lowest ordering energies are listed in Table 1 and shown in Figure 2.

Table 1. Cell configurations of lowest ordering energy ΔE_{Ckl}.

Cell Name n_{Ckl}	k Mn Atoms	l Al Atoms	ΔE_{Ckl} [eV]
n_{C08}	0	8	−1.2867
n_{C18}	1	8	−1.1524
n_{C28}	2	8	−1.0559
n_{C07}	0	7	−0.9304
n_{C68}	6	8	−0.9287
n_{C38}	3	8	−0.9233

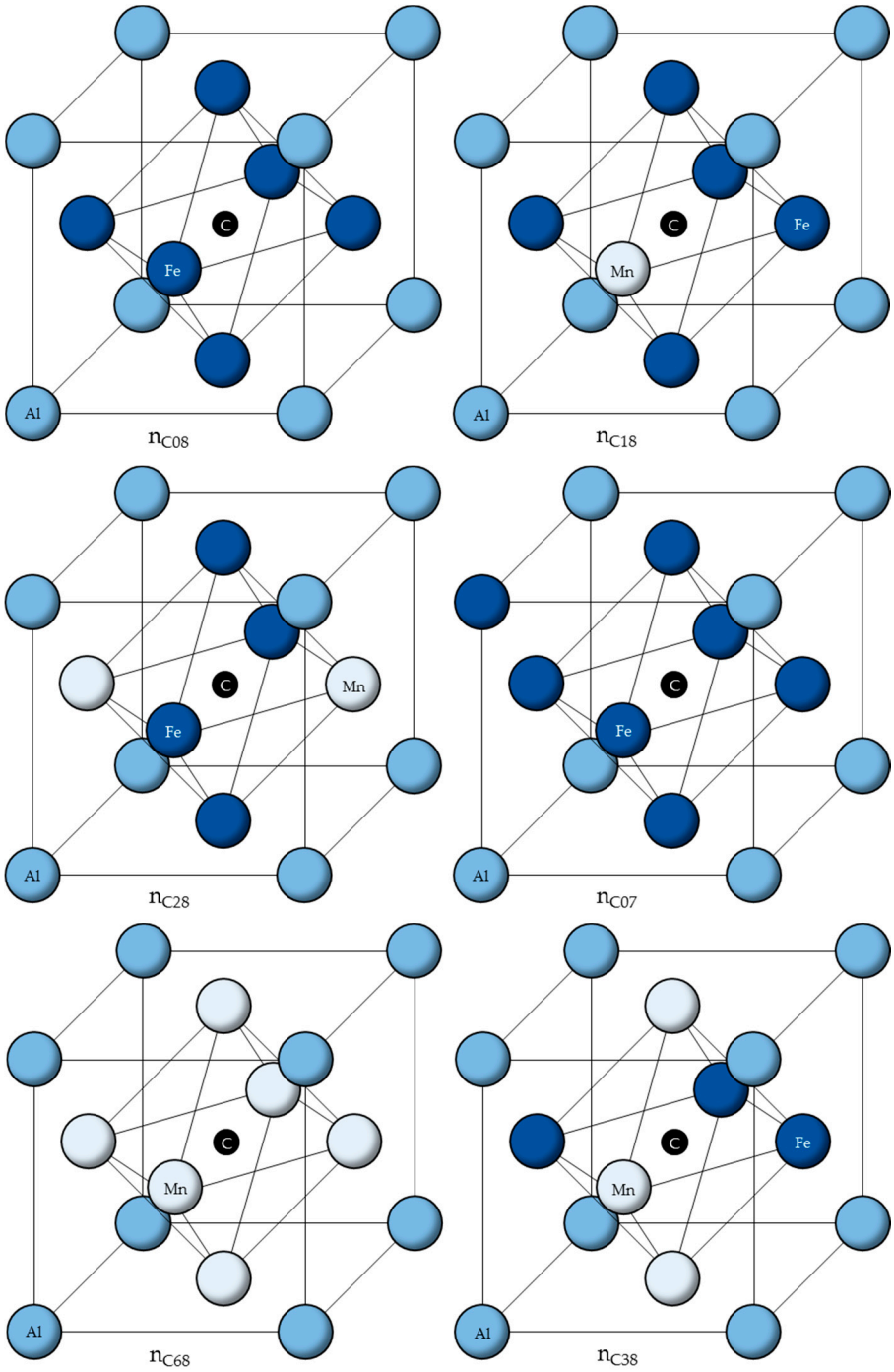

Figure 2. Energetically most favorable cell configurations.

In Equation (2), E_{random} describes the energy state of an unordered alloying system. In this case, a single carbon atom is situated in the central octahedral sites of a randomly chosen FCC-unit cell. This distribution is based on the assumption that there are no preferential octahedral sites, so neither the presence of Mn nor Al influences the position of carbon atoms. Thus, it can be assumed that, for the calculation of E_{random}, the likelihood of the presence of carbon is the same for each type of cell.

Using the random C distribution for E_{random}, E_{random} is calculated according to:

$$E_{random} = \sum_{k=0}^{14} \sum_{l=0}^{14} n_{Ckl,random} \Delta E_{Ckl}, \text{ for } k + l \leq 14 \text{ and } k, l \geq 0 \quad (7)$$

$$n_{Ckl,random} = n_{kl} \times \theta_C \tag{8}$$

Since $\sum n_{kl} = 1$, this method of determining $n_{Ckl,random}$ ensures that carbon is distributed homogeneously in the material, as well as ensuring that every available carbon atom is situated in an octahedral site of a cell.

Contrary to the homogeneous distribution of carbon for E_{random}, the distribution of C for the calculation of E_{SRO} is based on the calculated ordering energies [33]. Since the differences in ordering energy between different cell configurations are significant, as is shown in Table 1, it is assumed that carbon is always situated in the most favorable cell that has not already been assigned a carbon atom. Assuming that at higher temperatures, for example during recrystallization annealing, the diffusion of carbon as an interstitial alloying element is possible, carbon will diffuse to positions with minimal ordering energy in order to minimize the system's Gibbs energy. This means that the cells selected for saturation with carbon are the cells with the lowest ΔE_{Ckl} until $n_{Ckl,SRO} = \theta_C$.

The calculation of ordering energies in the model presented within this work was performed via ab initio simulations based on quantum-mechanical structure optimizations employing density-functional theory (DFT) within the Vienna ab initio Simulation Package (VASP) [33]. The quantum-mechanical structure optimizations are performed based on calculations of lowest-energy states of the electron structure and thus, are conducted at 0 K. Results from ab initio approaches employing DFT have offered good results that are in line with experimental evidence. For example, Mössbauer spectroscopy [17], atom-probe tomography (APT) [42], in situ synchrotron X-ray diffraction measurements [23], and correlative TEM/APT approaches [43] have shown that results from ab initio simulations employing DFT are applicable to systems containing nano-sized κ-carbides that are usually formed during isothermal annealing at temperatures of 600 °C and above. Generally speaking, the effect of temperature changes on the lattice parameter and on intrinsic material properties that derive from electron effects like electrical conductivity is often approximated to be linear [44]. The serrated flow curves of many high-manganese TWIP steels usually occur at temperatures of up to about 200 °C. At higher temperatures, this dynamic strain aging-like effect is either very small or is not detected at all [2,7].

In order to model the temperature dependence of σ_{SRO}, the ab initio results are fitted using a linear approximation of a decrease in σ_{SRO} between 0 K and 500 K. For this purpose, it is assumed that the fact that no serrated flow curve is expected at 500 K can be interpreted as a result of no significant strength increase by short-range ordered clusters.

Based on those assumptions and equations, $\sigma_{Y,calc}$ in MPa was calculated using Equations (2), (3), and (7) for 13 different HMnS with known average grain sizes d_m in µm, listed in Table 2. The alloying contents are given in wt. %.

Table 2. Chemical composition of HMnS used in this study in wt. %; grain size d_m in µm; experimentally determined and calculated yield strength $\sigma_{Y,exp}$ and $\sigma_{Y,calc}$ in MPa, experimental data of alloys marked with * are taken from [14].

Alloy	C	Mn	Al	d_m	$\sigma_{Y,exp}$	$\sigma_{Y,calc}$
X60MnAl17-1	0.56	17.00	1.35	8	328	356
X50MnAl15-1 *	0.49	15.40	1.30	27	294	281
X30MnAl22-1	0.33	22.46	1.21	18	277	275
X30MnAl17-1	0.32	16.80	1.47	17	255	276
X70Mn24	0.71	23.50	0.01	16	334	334
X60Mn23	0.57	23.21	0.01	10	328	334
X50Mn30 *	0.50	30.00	0.00	30	276	273
X50Mn22	0.54	21.95	0.00	14	328	311
X50Mn18 *	0.53	17.90	0.01	8	356	341
X30Mn28	0.28	28.00	0.00	9	291	294
X30Mn23	0.32	22.79	0.01	10	284	291
X30Mn22 *	0.31	22.28	0.00	3	381	384
X30Mn13 *	0.30	12.74	0.01	10	266	274

Experimental yield strength data was taken from the literature [5,14]. Additionally, quasistatic tensile tests have been carried out using a Zwick Z250 tensile testing machine of the AllroundLine by Zwick Roell (Ulm, Germany).

σ_{SS} has been calculated using a linear approximation to explain the differences between experimental and calculated values for the yield strength using the following equation that is a direct result of Equation (1):

$$\sigma_{SS,exp} = \sigma_{Y,exp} - \sigma_{\gamma-Fe} - \sigma_{GS} - \sigma_{SRO} \tag{9}$$

This way, $\sigma_{SS,exp}$ was determined for all steels in Table 2. A regression analysis was performed with respect to the alloying contents of C, Mn, and Al.

The regression analysis lead to the following equation to calculate σ_{SS} with respect to the alloying contents χ_i in weight percent:

$$\sigma_{SS} = 84.55\chi_C + 1.35\chi_{Mn} + 0.44\chi_{Al} \tag{10}$$

Overall, the lattice distortion effect of carbon is by far the strongest contribution to solid solution hardening. This is in accordance with calculations of the misfit of C in an octahedral site using the crystallographic correlation $\frac{r_{OL}}{r_{Fe}} = 0.41$. Comparing the size of the octahedral site to the size of a carbon atom shows that a carbon atom is approximately 8% bigger than the octahedral site, leading to a lattice distortion. Using the lattice parameter calculated according to Equation (3), this size difference can be calculated to approximately 0.03 nm. Comparing this value with the lattice distortion effects by Al and Mn in an austenitic steel according to [45], which are 0.000065 $\frac{nm}{wt.\ \%\ Mn}$ and 0.00095 $\frac{nm}{wt.\ \%\ Al}$ respectively, the difference in contributions between C and Mn and Al in Equation (10) appear to be reasonable.

3. Results and Discussion

Figure 3 shows that the calculations for the yield strength $\sigma_{Y,calc}$ using the proposed model show good agreement with the experimental data.

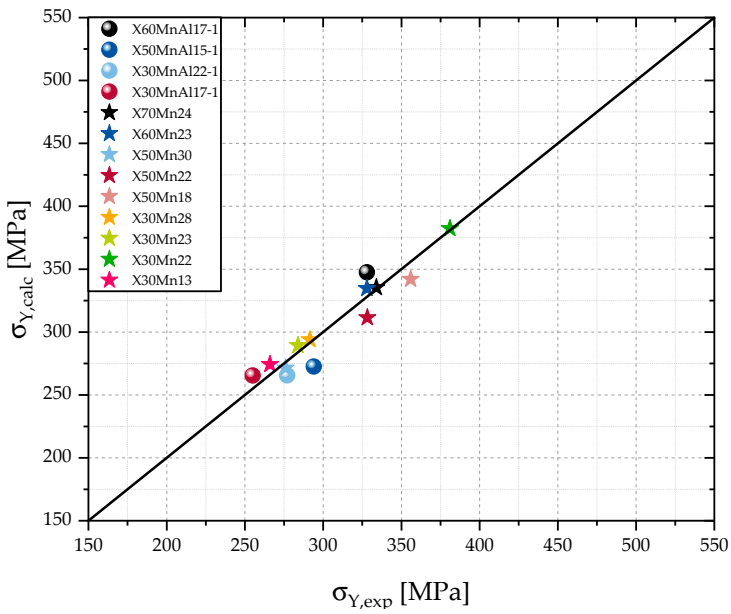

Figure 3. Comparison of calculated and experimental values for σ_Y.

The calculations used in this work lead to differences between $\sigma_{Y,calc}$ and $\sigma_{Y,exp}$ that are smaller than 10%. Those small differences between $\sigma_{Y,calc}$ and $\sigma_{Y,exp}$ might be a result of a negligence of other

alloying elements that participate in solid solution hardening, minor inaccuracies of the measurement of the alloying contents, or d_m.

Since σ_{SRO} can also be understood as a deviation from linear solid solution hardening behavior, a close relationship between σ_{SS} and σ_{SRO} seems logical. Higher alloying contents of C, Mn, and Al lead to a higher solid solution strengthening, but also to more carbon atoms integrated in Mn-C, Al-C, and Mn-Al-C clusters, as well as a higher amount of cells with more Al atoms in the second coordination sphere or Mn atoms in the first coordination sphere according to Equation (5).

The individual contributions of solid solution hardening σ_{SS} and σ_{SRO} are illustrated in Figure 4.

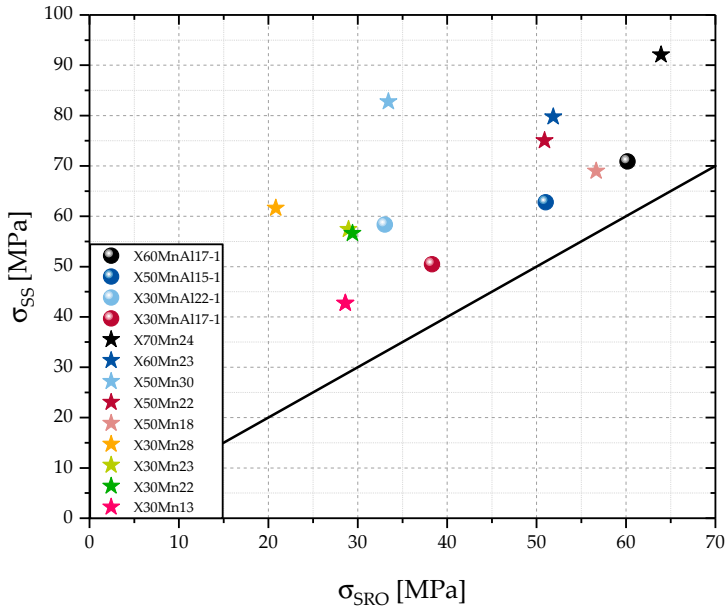

Figure 4. Contributions of σ_{SS} and σ_{SRO} to yield strength.

The strengthening effect of short-range ordered clusters σ_{SRO} is dependent on the chemical composition. For the steel compositions analyzed within the scope of this work, σ_{SRO} at room temperature is approximately in the range of 20 MPa for X30Mn28, containing 0.28 wt. % C and 28.00 wt. % Mn, and 65 MPa for X60MnAl17-1, containing 0.56 wt. % C, 17.00 wt. % Mn, and 1.35 wt. % Al.

Based on Figure 4, one could think, that the connection between σ_{SS} and σ_{SRO} is approximately linear. However, it needs to be kept in mind that the calculation of σ_{SS} is based on linear approximations as well. Additionally, it should be pointed out that although the contribution of σ_{SS} to σ_Y is always greater than that of σ_{SRO}, the proportion between σ_{SS} and σ_{SRO} does not seem to follow a linear trend based on chemical composition. This is illustrated by the line in Figure 4 that represents a relation of $\frac{\sigma_{SS}}{\sigma_{SRO}} = 1$. To further point out the differences in the contributions to σ_Y, the individual contributions of σ_{GS}, σ_{SS}, and σ_{SRO} are portrayed in Figure 5.

According to Figure 5, the contribution of σ_{SRO} to σ_Y is significant. The proportional contribution of σ_{SRO} to σ_Y is in the range of 7.1% for X30Mn28 up to 19.1% for X70Mn24. Since a grain size effect on σ_{SRO} is not assumed in this work, the impact of σ_{SRO} for a given steel composition with larger grain size is higher than for the same steel composition with finer grains. Correspondingly, the proportional contribution of σ_{SRO} that is portrayed in Figure 5 is higher for compositions with larger grains and thus, with smaller grain size strengthening effects σ_{GS}.

The comparison of σ_{SS} and σ_{SRO} for the steels X30Mn13 and X30Mn22 could lead to the conclusion that an increase in Mn content does not significantly influence σ_{SRO}. On the other hand, by comparing X30Mn22 with X30Mn28, it does appear that Mn actually reduces σ_{SRO}. Accordingly, based on these calculations, no clear tendency of the impact of a single alloying element on σ_{SRO} can be found.

For a more detailed analysis, the impact of C and Mn on σ_{SRO} is portrayed in Figures 6 and 7 with regards to the development of σ_{SRO}, σ_{SS}, E_{random}, and E_{SRO} for steels with and without Al.

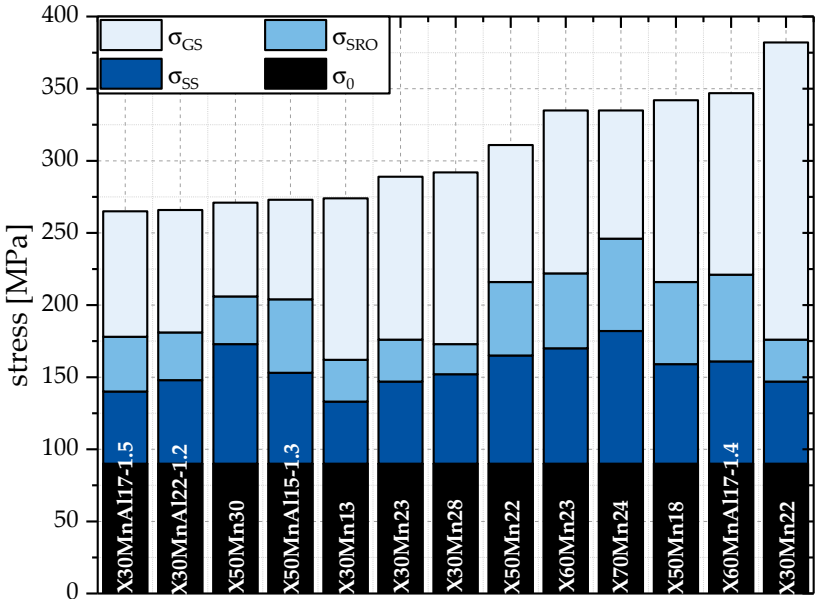

Figure 5. Proportional contribution of σ_{SS}, σ_{SRO}, and σ_{GS} to σ_Y.

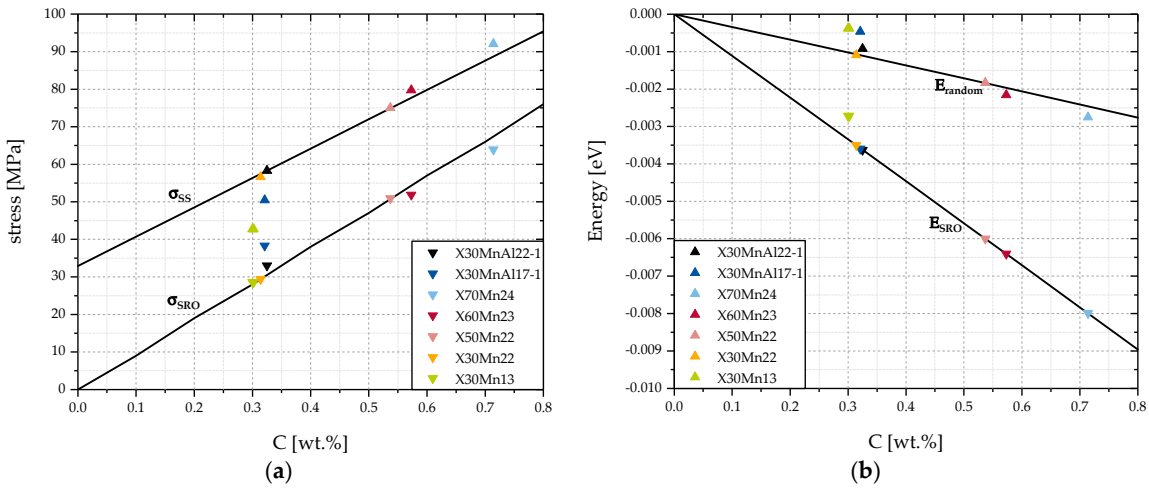

Figure 6. Impact of C on (**a**) σ_{SRO}, σ_{SS}; and (**b**) E_{random} and E_{SRO}.

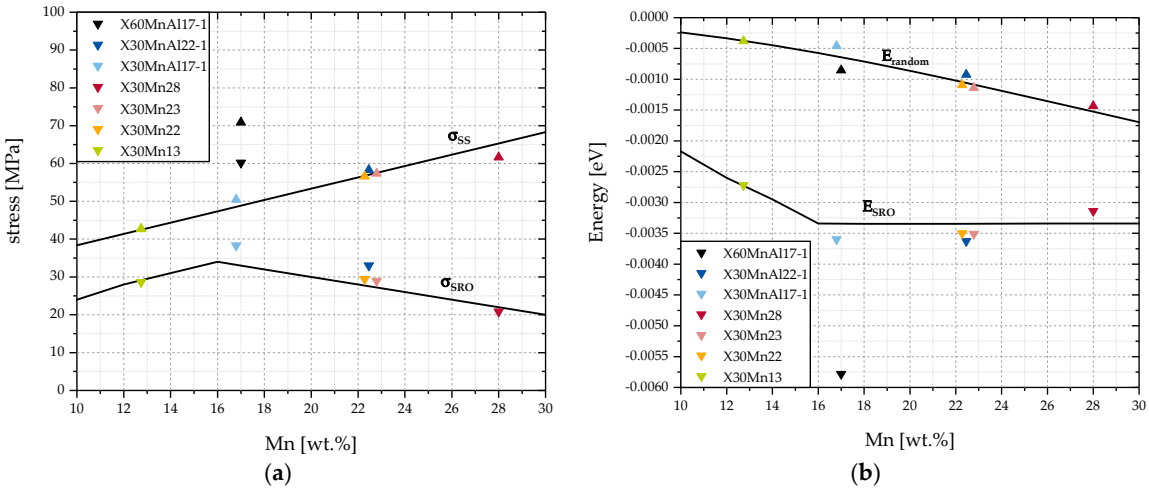

Figure 7. Impact of Mn on (**a**) σ_{SRO}, σ_{SS}; and (**b**) E_{random} and E_{SRO}.

Figure 6 analyzes a steel with a constant Mn content of 22 wt. % with increasing C content from 0.0 wt. % up to 0.8 wt. %. Additionally, seven steels that were studied in this work were selected to illustrate the impact of changes in Mn content and Al content.

According to Figure 6a, σ_{SRO} and σ_{SS} increase approximately linearly with C content. This can be explained by an increasing number of cells with carbon atoms. In theory, this increase in σ_{SRO} will only occur as long as there are cells with a preferential structure available, which leads to a decrease in ordering energy E_{SRO}, as can be seen in Figure 6b. If no preferential cells were available, C atoms would have to be situated in non-preferential cells with $\Delta E_{Ckl} > 0$ eV. To a small degree, this effect is included in the calculation of E_{random} because C is assumed to be homogeneously distributed among all cells, including those with positive and, thus, unfavorable values of ΔE_{Ckl}. This explains the lower rate of decrease of E_{random} in Figure 6b compared to E_{SRO}. However, σ_{SRO} will always remain positive because, according to Equation (2), as long as E_{random} is bigger than E_{SRO}, σ_{SRO} will be positive. This premise is always fulfilled by using the assumption in this work, that carbon will be situated in the cells of lowest possible ordering energy first and that the distribution of alloying elements for the calculation of E_{random} and E_{SRO} is the same.

Looking at Figure 6a, the steels with Al, X30MnAl22-1 and X30MnAl17-1, show positive deviations for the calculated values of σ_{SRO} and X30MnAl17-1 shows a negative deviation for σ_{SS}. In the case of solid solution strengthening for X30MnAl17-1, this can be explained by the low Mn content of 16.80 wt. % compared to the 22.00 wt. % used as a basis of calculation of σ_{SS} in Figure 6. Accordingly, X70Mn24 and X60Mn23 show slightly higher values for than σ_{SS} it would be the case for 22.00 wt. % Mn.

The increase of σ_{SRO} can be explained by the impact of the introduction of new cell configurations containing Al atoms. According to Table 1, n_{C08} is the lowest possible energy configuration. However, since the Al content of the steels in this study is very low, only very few cells with the configuration n_{C08} are available. The majority of Al atoms is in cells also containing Mn atoms. According to [33], the introduction of Al atoms as a 2NN into cells with Mn atoms as 1NN does not necessarily lead to a lower ordering energy, but is rather dependent of the number of 1NN Mn atoms. The molar fraction of Mn in a steel containing 22 wt. % Mn obviously depends on the wt. % of the other alloying elements. For the X30MnAl22-1, the molar fraction of Mn is approximately 0.23. According to Equation (5), the most common cell configuration is expected to be n_{30}. The ordering energy of the cell configuration n_{C30} is $\Delta E_{C30} = -0.0501$ eV. This means that this cell configuration is preferential to a pure iron FCC-unit cell. Increasing the number of Al atoms in this cell configuration to 1 and 2 respectively results in $\Delta E_{C31} = -0.0082$ eV and $\Delta E_{C32} = 0.0338$ eV. Both cell configurations are not preferential with respect to n_{C30} which according to previous assumptions means that the cells n_{C31} and

n_{C32} will not contain a carbon atom as long as there are other more preferential cell configurations like n_{30} that do not already contain a carbon atom. In turn, E_{SRO} will not be negatively influenced by cell configurations like n_{C31} and n_{C32}. However, E_{random} will include the negative impact of unfavorable cell configurations which will lead to an increase of E_{random} and a total increase of σ_{SRO}.

Overall, it can be said that the positive impact of Al on σ_{SRO} is a result of an introduction of favorable cell configurations containing Al atoms that inhibit a carbon atom and the avoidance of cell configurations of unfavorable cell configurations.

Figure 7 analyzes a steel with a constant C content of 0.3 wt. % with increasing Mn content from 10 wt. % up to 30 wt. %. Seven steels with varying Al and C content were added to the diagram.

Contrary to the impact of C that is documented in Figure 6, a local maximum of σ_{SRO} at approximately 16 wt. % Mn is observed. Looking at Figure 7b, this can be explained by the stagnation of E_{SRO} for Mn contents of 16 wt. % and higher. At the same time, E_{random} is decreasing, leading to a smaller difference between E_{random} and E_{SRO} and accordingly to a lower σ_{SRO}.

The stagnation of E_{SRO} can be explained by considering the method of calculation for σ_{SRO}. For Al-free steels, the energetically optimal cell is n_{60}. As long as $\theta_C < n_{C60}$, an increase in the amount of C atoms will decrease E_{SRO}. This is due to the underlying assumption that C atoms will be situated in preferential cells of lowest possible ordering energy. At $\theta_C = n_{C60}$, all C atoms are situated in cells of optimal configuration and thus, E_{SRO} is minimized. Due to the way E_{random} is calculated in Equation (7), E_{random} continues to decrease at $\theta_C > n_{C60}$. As a result, σ_{SRO} decreases.

In accordance with Figure 6a, Figure 7a shows that additions of Al and C increase σ_{SRO} significantly.

The contribution of solid solution hardening σ_{SS} increases linearly with the Mn and C content, as it is to be expected considering Equation (10).

To conclude, unlike for the addition of C, Mn additions do not always increase σ_{SRO}. This is a result of a stagnation of E_{SRO} because of a saturation of preferential cells with carbon. In theory, the same effect should be noticeable for C and Al, as well. However, because of the comparably low alloying contents of those elements, it is very unlikely that a point of saturation will be reached in common alloys.

This decrease in σ_{SRO} can be understood as the impact of the deviation from linear solid solution hardening. If the ratio of Mn atoms to Fe atoms becomes increasingly larger and the amount of cells with randomly-distributed Mn increases, the impact of an actual ordering of Mn decreases since fewer cells are brought into short-range ordering to minimize the ordering energy.

Overall, the change of E_{Order} with varying contents of alloying elements can be understood as the effectiveness of an alloy addition of those elements with respect to the increase in strength by short-range ordering. Since it is assumed that σ_{SS} follows a linear trend and σ_{GS} is fixed, $\left|\frac{\delta E_{Order}}{\delta \chi_i}\right|$ is an indicator for the effectiveness of an addition of an alloying element. A higher $\left|\frac{\delta E_{Order}}{\delta \chi_i}\right|$ means a greater efficiency in employing an addition of the alloying element i. Looking at Figures 6 and 7, C and Al both appear to be more efficient than Mn in increasing the yield strength by short-range ordering.

In order to compare the accuracy of the model used in this work to calculate σ_Y with other descriptive models, $\sigma_{Y,model}$ according to models by Pickering [15], Lorenz [15], Bouaziz [11], De Cooman [2], and Choi [46] has been calculated. The equations used for $\sigma_{Y,model}$ are listed in Table 3. The coefficients used for the alloying contents are in $\frac{\text{MPa}}{\text{wt. \%}}$, coefficients for grain size influence are in MPam$^{0.5}$ unless stated otherwise. It needs to be pointed out that although all of the models are for austenitic steels, only the models of Bouaziz, De Cooman, and Choi are specifically for HMnS. Additionally, some of the models include coefficients for the Hall-Petch effect while others neglect them. In order to be able to compare the models, the grain size effect has been calculated according to Equation (4) and added to the model calculations of Choi and Bouaziz.

Table 3. Solid solution hardening models in the literature.

Model	$\sigma_{Y,model}$
Pickering	$68 + 493N + 354C + 3.7Cr + 14Mo + 20Si + 0.22d^{-1/2}$
Lorenz	$40 + 450N + 525C + 2Mn + 8.4Cr + 22Mo + 5Cu + 0.77d^{-1/2}$
Bouaziz	$228 + 137C - 2Mn + \sigma_{GS}$
De Cooman	$189 + 413/\sqrt{(d[\mu m])}$
Choi	$97 + 279C - 1.5Mn + 49.6Si + 20.5Al + \sigma_{GS}$

Figure 8 compares $\sigma_{Y,model}$ with $\sigma_{Y,calc}$ and $\sigma_{Y,exp}$.

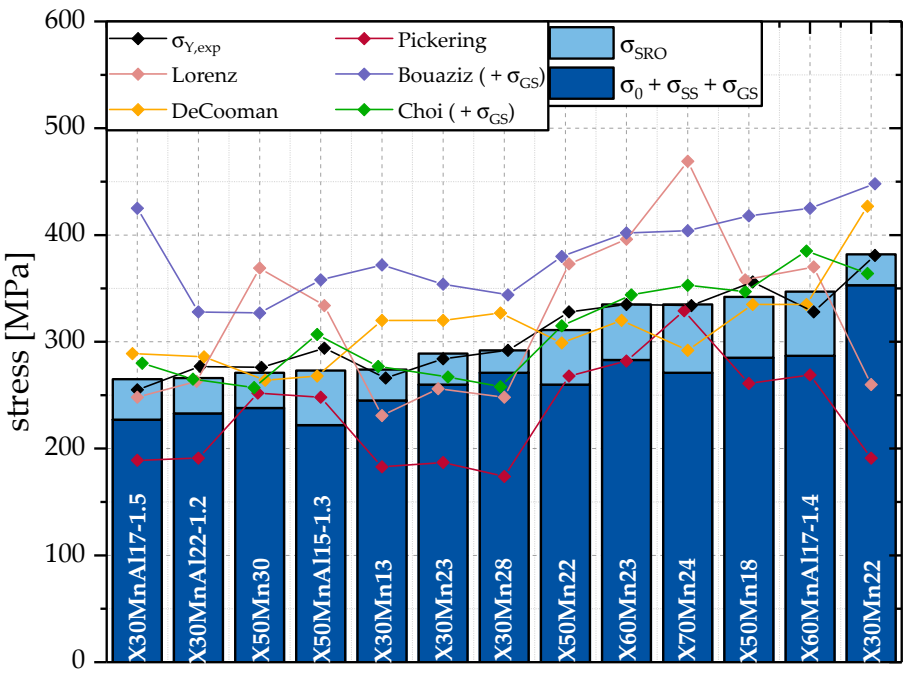

Figure 8. Comparison of models of σ_Y for the steels used in this paper.

Due to the difference in the steel concepts those models were developed for, significant deviations from $\sigma_{Y,exp}$ can be seen. Those deviations are a result of a focus on other alloying elements. For example, Pickering does not consider the impact of Mn on yield strength. Nevertheless, the models of Choi [46] and De Cooman [2] offer reasonable results, but are not as close to the experimental data as the model developed in this work. Additionally, the model by De Cooman does not take compositional variances into account, while the model of Choi considers the impact of Mn on yield strength to be negative.

The models of Pickering and Lorenz are not applicable to HMnS based on the results of the calculations. The model by Bouaziz tends to overestimate the yield strength.

4. Conclusions

A basic ab initio-based model for the calculation of σ_Y has been developed. The model shows good agreement with the experimental values. Discrepancies between experimental $\sigma_{Y,exp}$ and calculation results $\sigma_{Y,calc}$ are smaller than 10%. While many complexity-reducing assumptions have been made that lead to inaccuracies when calculating σ_{SRO}, this model portrays that the general concept of combining ab initio simulations with experimental data can lead to feasible results on a macroscopic scale. This is also shown by the calculated positive impact of Mn and Al on yield strength by solid solution strengthening in a reasonable range.

The impact of the alloying content of C, Mn, and Al on the strengthening by short-range ordering was analyzed. For the given steel compositions with fully austenitic microstructures in this work,

the values for σ_{SRO} are as high as approximately 65 MPa. This significant strengthening leads to a proportional contribution to σ_Y of nearly 20%.

While an increase in C and Al increases σ_{SRO} as long as a sufficient number of atoms of substitutional alloying elements are available to form preferential cell structures, a limiting factor for the effectiveness of strength increases by Mn was found.

The impact of short-range ordered clusters during deformation needs to be evaluated. A higher amount of more stable, energetically favorable clusters might not only lead to an increase in σ_{SRO} and σ_Y, it might also impact the beginning of serrations in the flow curve, as well as their amplitude if the serrations are resulting from short-distance carbon atom jumps associated with the cutting of clusters.

Acknowledgments: The authors are thankful for the financial support from Deutsche Forschungsgemeinschaft (DFG) within the Project C2: "Material Properties of High Mn-Steels" of the Collaborative Research Centre (SFB) 761 "Steel-ab initio". The provision of experimental data by Sebastian Wesselmecking (Steel Institute, RWTH Aachen University) is very much appreciated as well as the provision of ab initio calculation results by Dronskowski, Tobias Timmerscheidt, and Dmitri Bogdanovski (Department of Inorganic Chemistry, RWTH Aachen University) of Project A1: "ab initio Quantum chemistry of the Fe-Mn-C system" of SFB 761 "Steel-ab initio".

Author Contributions: Simon Sevsek analyzed the data. Simon Sevsek and Wolfgang Bleck wrote the paper.

Conflicts of Interest: The authors declare no conflict of interest.

References

1. De Cooman, B.C.; Kwon, O.; Chin, K.-G. State-of-the-knowledge on TWIP steel. *Mater. Sci. Technol.* **2012**, *28*, 513–527. [CrossRef]
2. De Cooman, B.C. High Mn TWIP steel and medium Mn steel. In *Automotive Steels: Design, Metallurgy, Processing and Applications*, 1st ed.; Rana, R., Singh, S.B., Eds.; Woodhead Publishing: Cambridge, UK, 2017; pp. 317–385. ISBN 9780081006382.
3. Haase, C.; Ingendahl, T.; Güvenc, O.; Bambach, M.; Bleck, W.; Molodov, D.A.; Barrales-Mora, L.A. On the applicability of recovery-annealed Twinning-Induced Plasticity steels: Potential and limitations. *Mater. Sci. Eng. A* **2016**, *649*, 74–84. [CrossRef]
4. Abbasi, A.; Dick, A.; Hickel, T.; Neugebauer, J. First-principles investigation of the effect of carbon on the stacking fault energy of Fe–C alloys. *Acta Mater.* **2011**, *59*, 3041–3048. [CrossRef]
5. Bouaziz, O.; Zurob, H.; Chehab, B.; Embury, J.D.; Allain, S.; Huang, M. Effect of chemical composition on work hardening of Fe–Mn–C TWIP steels. *Mater. Sci. Technol.* **2011**, *27*, 707–709. [CrossRef]
6. Tewary, N.K.; Ghosh, S.K.; Chatterjee, S. Effect of Al Content in Low Carbon High Manganese TWIP Steel. *Key Eng. Mater.* **2016**, *706*, 16–22. [CrossRef]
7. Bäumer, A.; Jimenez, J.A.; Bleck, W. Effect of temperature and strain rate on strain hardening and deformation mechanisms of high manganese austenitic steels. *Int. J. Mater. Res.* **2010**, *101*, 705–714. [CrossRef]
8. Choi, K.; Seo, C.-H.; Lee, H.; Kim, S.K.; Kwak, J.H.; Chin, K.G.; Park, K.-T.; Kim, N.J. Effect of aging on the microstructure and deformation behavior of austenite base lightweight Fe–28Mn–9Al–0.8C steel. *Scr. Mater.* **2010**, *63*, 1028–1031. [CrossRef]
9. Gutierrez-Urrutia, I.; Raabe, D. Microbanding mechanism in an Fe–Mn–C high-Mn twinning-induced plasticity steel. *Scr. Mater.* **2013**, *69*, 53–56. [CrossRef]
10. Liu, F.; Dan, W.J.; Zhang, W.G. Strain hardening model of TWIP steels with manganese content. *Mater. Sci. Eng. A* **2016**, *674*, 178–185. [CrossRef]
11. Bouaziz, O.; Allain, S.; Scott, C.P.; Cugy, P.; Barbier, D. High manganese austenitic twinning induced plasticity steels: A review of the microstructure properties relationships. *Curr. Opin. Solid State Mater. Sci.* **2011**, *15*, 141–168. [CrossRef]
12. Bouaziz, O. Strain-hardening of twinning-induced plasticity steels. *Scr. Mater.* **2012**, *66*, 982–985. [CrossRef]
13. Ohkubo, N.; Miyakusu, K.; Uematsu, Y.; Kimura, H. Effect of Alloying Elements on the Mechanical Properties of the Stable Austenitic Stainless Steel. *ISIJ Int.* **1994**, *34*, 764–772. [CrossRef]
14. Kang, J.-H.; Ingendahl, T.; von Appen, J.; Dronskowski, R.; Bleck, W. Impact of short-range ordering on yield strength of high manganese austenitic steels. *Mater. Sci. Eng. A* **2014**, *614*, 122–128. [CrossRef]
15. Sieurin, H.; Zander, J.; Sandström, R. Modelling solid solution hardening in stainless steels. *Mater. Sci. Eng. A* **2006**, *415*, 66–71. [CrossRef]

16. Oda, K.; Fujimura, H.; Ino, H. Local interactions in carbon-carbon and carbon-M (M: Al, Mn, Ni) atomic paris in FCC gamma-iron. *J. Phys. Condens. Matter* **1994**, *6*, 679–692. [CrossRef]
17. Bentley, A.P. Ordering in Fe–Mn–Al–C austenite. *J. Mater. Sci. Lett.* **1986**, *5*, 907–908. [CrossRef]
18. McLellan, R.B.; Dunn, W.W. A quasi-chemical treatment of interstitial solid solutions: It application to carbon austenite. *J. Phys. Chem. Solids* **1969**, *30*, 2631–2637. [CrossRef]
19. Pelton, A.D.; Kang, Y.-B. Modeling short-range ordering in solutions. *Int. J. Mater. Res.* **2007**, *98*, 907–917. [CrossRef]
20. Honeycombe, R.W.K. The effect of temperature and alloying additions on the deformation of metal crystals. *Progress Mater. Sci.* **1961**, *9*, 95–120. [CrossRef]
21. Oda, K.; Kondo, N.; Shibata, K. X-ray Absorption Fine Structure Analysis of Interstitial (C, N)-Substitutional (Cr) Complexes in Austenitic Stainless Steels. *ISIJ Int.* **1990**, *30*, 625–631. [CrossRef]
22. Von Appen, J.; Dronskowski, R. Carbon-Induced Ordering in Manganese-Rich Austenite—A Density-Functional Total-Energy and Chemical-Bonding Study. *Steel Res. Int.* **2011**, *82*, 101–107. [CrossRef]
23. Song, W.; Zhang, W.; von Appen, J.; Dronskowski, R.; Bleck, W. k-Phase Formation in Fe–Mn–Al–C Austenitic Steels. *Steel Res. Int.* **2015**, *86*, 1161–1169. [CrossRef]
24. Raabe, D.; Roters, F.; Neugebauer, J.; Gutierrez-Urrutia, I.; Hickel, T.; Bleck, W.; Schneider, J.M.; Wittig, J.E.; Mayer, J. Ab initio-guided design of twinning-induced plasticity steels. *MRS Bull.* **2016**, *41*, 320–325. [CrossRef]
25. Medvedeva, N.I.; Park, M.S.; van Aken, D.C.; Medvedeva, J.E. First-principles study of Mn, Al and C distribution and their effect on stacking fault energies in fcc Fe. *J. Alloys Compd.* **2014**, *582*, 475–482. [CrossRef]
26. Timmerscheidt, T.; Dey, P.; Bogdanovski, D.; von Appen, J.; Hickel, T.; Neugebauer, J.; Dronskowski, R. The Role of κ-Carbides as Hydrogen Traps in High-Mn Steels. *Metals* **2017**, *7*, 264. [CrossRef]
27. McLellan, R.B. Cell models for interstitial solid solutions. *Acta Metall.* **1982**, *30*, 317–322. [CrossRef]
28. Bhadeshia, H.K.D.H. Diffusion of carbon in austenite. *Met. Sci.* **1981**, *15*, 477–479. [CrossRef]
29. McLellan, R.B.; Ko, C. The C–C interaction energy in iron-carbon solid solutions. *Acta Metall.* **1987**, *35*, 2151–2156. [CrossRef]
30. McLellan, R.B.; Ko, C. The diffusion of carbon in austenite. *Acta Metall.* **1988**, *36*, 531–537. [CrossRef]
31. Gholizadeh, H.; Draxl, C.; Puschnig, P. The influence of interstitial carbon on the g-surface in austenite. *Acta Metall.* **2013**, *61*, 341–349. [CrossRef]
32. Lee, S.-J.; Kim, J.; Kane, S.N.; DeCooman, B.C. On the origin of dynamic strain aging in twinning-induced plasticity steels. *Acta Metall.* **2011**, *59*, 6809–6819. [CrossRef]
33. Timmerscheidt, T.; Dronskowski, R. An Ab Initio Study of Carbon-Induced Ordering in Austenitic Fe–Mn–Al–C Alloys. *Steel Res. Int.* **2017**, *88*, 1–10. [CrossRef]
34. Sumin, V.V.; Chimid, G.; Rashev, T.; Saryivanov, L. The Neutron-Spectroscopy Proof of the Strong Cr–N Interactions in Nitrogen Stainless Steels. *Mater. Sci. Forum* **1999**, *318–320*, 31–40. [CrossRef]
35. Bouaziz, O.; Barbier, D. Benefits of Recovery and partial Recrystallization of Nano-Twinned Austenitic Steels. *Adv. Eng. Mater.* **2013**, *15*, 976–979. [CrossRef]
36. Fiore, N.F.; Bauer, C.L. Binding of solute atoms to dislocations. *Progress Mater. Sci.* **1968**, *13*, 85–134. [CrossRef]
37. Butt, M.Z.; Feltham, P. Solid-solution hardening. *J. Mater. Sci.* **1993**, *28*, 2557–2576. [CrossRef]
38. Saeed-Akbari, A.; Imlau, J.; Prahl, U.; Bleck, W. Derivation and Variation in Composition-Dependent Stacking Fault Energy Maps Based on Subregular Solution Model in High-Manganese Steels. *Metall. Mater. Trans. A* **2009**, *40*, 3076–3090. [CrossRef]
39. Kang, J.-H.; Duan, S.; Kim, S.-J.; Bleck, W. Grain Boundary Strengthening in High Mn Austenitic Steels. *Metall. Mater. Trans. A* **2016**, *47*, 1918–1921. [CrossRef]
40. Kang, S.; Jung, Y.-S.; Jun, J.-H.; Lee, Y.-K. Effects of recrystallization annealing temperature on carbide precipitation, microstructure and mechanical properties in Fe–18Mn–0.6C–1.5Al TWIP steel. *Mater. Sci. Eng. A* **2010**, *527*, 745–751. [CrossRef]
41. De las Cuevas, F.; Reis, M.; Ferraiuolo, A.; Pratolongo, G.; Karjalainen, L.P.; Alkorta, J.; Gil Sevillano, J. Hall-Petch relationship of a TWIP steel. *Key Eng. Mater.* **2010**, *423*, 147–152. [CrossRef]
42. Bartlett, L.N.; van Aken, D.C.; Medvedeva, J.; Isheim, D.; Medvedeva, N.I.; Song, K. An Atom Probe Study of Kappa Carbide Precipitation and the Effect of Silicon Addition. *Metall. Mater. Trans. A* **2014**, *45*, 2421–2435. [CrossRef]

43. Yao, M.J.; Welsch, E.; Ponge, D.; Haghighat, S.; Sandlöbes, S.; Choi, P.; Herbig, M.; Bleskov, I.; Hickel, T.; Lipinska-Chwalek, M.; et al. Strengthening and strain hardening mechanisms in a precipitation-hardened high-Mn lightweight steel. *Acta Mater.* **2017**, *140*, 258–273. [CrossRef]
44. Gottstein, G. *Physikalische Grundlagen der Materialkunde*, 3rd ed.; Springer: Berlin/Heidelberg, Germany, 2007; ISBN 978-3-540-71104-9.
45. Li, M.; Chang, H.; Kao, P.; Gan, D. The effect of Mn and Al contents on the solvus of κ phase in austenitic Fe–Mn–Al–C alloys. *Mater. Chem. Phys.* **1999**, *59*, 96–99. [CrossRef]
46. Choi, W.S.; de Cooman, B.C.; Sandlöbes, S.; Raabe, D. Size and orientation effects in partial dislocation-mediated deformation of twinning-induced plasticity steel micro-pillars. *Acta Mater.* **2015**, *98*, 391–404. [CrossRef]

© 2018 by the authors. Licensee MDPI, Basel, Switzerland. This article is an open access article distributed under the terms and conditions of the Creative Commons Attribution (CC BY) license (http://creativecommons.org/licenses/by/4.0/).